A reconstruction algorithm for thermoacoustic tomography with compensation for acoustic speed heterogeneity

IOP PUBLISHING PHYSICS IN MEDICINE AND BIOLOGY

Phys. Med. Biol. **53** (2008) 4971–4982 doi:10.1088/0031-9155/53/18/008

A reconstruction algorithm for thermoacoustic tomography with compensation for acoustic speed heterogeneity

Chi Zhang and Yuanyuan Wang

Department of Electronic Engineering, Fudan University, Shanghai 200433, People's Republic of China

E-mail: yywang@fudan.edu.cn

Received 9 May 2008, in final form 30 June 2008
Published 18 August 2008
Online at stacks.iop.org/PMB/53/4971

Abstract

An inverse reconstruction algorithm for thermoacoustic tomography (TAT) is proposed with the compensation for the acoustic speed heterogeneity. Not requiring the prior knowledge of the acoustic speed distribution like most other algorithms, this algorithm utilizes the correlation information between thermoacoustic signals to compensate for the acoustic heterogeneity. The absorbed energy density is reconstructed on the basis of a corrected time-domain formula. Computer simulations are carried out to validate the algorithm. It is shown that the algorithm has a good precision within the acoustic speed variation of 10%, strong robustness to random data noises and good computational efficiency compared to other model-based methods. Therefore, the algorithm may be used in TAT of biological soft tissues, in which the acoustic speed variation is normally within 10%.

1. Introduction

Thermoacoustic tomography (TAT), which is also often referred to as photoacoustic tomography (PAT), is emerging as a potential technique of noninvasive medical imaging (Kruger *et al* 2000, Niederhauser *et al* 2005, Wang *et al* 2003, Xu and Wang 2006, Zhang *et al* 2006). TAT combines the high contrast of optical imaging and the high resolution of ultrasound imaging, and has shown potential in tumor detection (Guo *et al* 2007, Kruger *et al* 2000), blood vessel imaging (Niederhauser *et al* 2005), brain functional imaging (Wang *et al* 2003) and blood flow measurement (Fang *et al* 2007).

Within TAT, biological tissues are irradiated by a short-pulsed electromagnetic wave (usually microwave or laser) and then generate thermoacoustic waves due to the thermoelastic expansion. Detected by the ultrasonic transducer, thermoacoustic waves can be used to reconstruct the absorbed energy density of the tissue. The reconstruction algorithm is a typical

inverse problem. Until now, many algorithms have been proposed (Anastasio *et al* 2005b, Kostli and Beard 2003, Kruger *et al* 1995, Kunyansky 2007, Xu *et al* 2003), most of which are based on the assumption that the acoustic speed is homogeneous in the tissue. However, this assumption is not tenable in some applications, such as breast imaging in which the acoustic speed variation can be as large as 10% (Xu and Wang 2003). In these cases, the reconstructed image will be deteriorated by blurring and displacement (Jin and Wang 2006, Xu and Wang 2003).

In recent years, several TAT algorithms with the correction for acoustic speed variations have been proposed (Anastasio *et al* 2005a, Jiang *et al* 2006, Jin and Wang 2006, Zhang and Anastasio 2006). Most of these algorithms need prior knowledge of the acoustic speed distribution (Anastasio *et al* 2005a, Jin and Wang 2006), which is obtained using other modalities (such as ultrasonic tomography), or suppose that the interface geometry of the acoustic speed distribution is in accordance with that of the electromagnetic absorption distribution (Zhang and Anastasio 2006), which may not always hold true. To the best of our knowledge, so far only one algorithm, based on the finite-element (FE) method, has been proposed without prior knowledge of the acoustic speed distribution (Jiang *et al* 2006). The FE-based method could reconstruct low frequency images of both the absorbed energy density and the acoustic speed distribution simultaneously. Yet, the FE method is computationally inefficient because of the fact that it is based on a forward model and uses iterative methods for updating the image.

In this paper, an inverse reconstruction algorithm with the compensation for the acoustic speed heterogeneity is proposed for TAT in the spherical measurement geometry. The algorithm employs the correlation between detected thermoacoustic signals to compensate for the acoustic heterogeneity, and can reconstruct the image very quickly without iterations. Moreover, it does not require prior knowledge of the acoustic speed distribution, and is therefore conveniently available in practical applications. Simulation studies are carried out to validate the algorithm.

2. Reconstruction algorithm

2.1. Inverse formula

In TAT, the electromagnetic pulse duration is much shorter than the thermal diffusion time, so the effect of the thermal diffusion can be ignored. The basic equation of three-dimensional TAT is given by Jin and Wang (2006), Xu *et al* (2003):

$$\nabla^2 p(\mathbf{r}, t) - \frac{1}{c(\mathbf{r})^2} \frac{\partial^2 p(\mathbf{r}, t)}{\partial t^2} = -\frac{\beta}{C_p} A(\mathbf{r}) \cdot \frac{\partial I(t)}{\partial t} \tag{1}$$

where $p(\mathbf{r}, t)$ is the acoustic pressure at the position $\mathbf{r}$, $A(\mathbf{r})$ is the absorbed energy density, t is the time, $I(t)$ is the electromagnetic pulse function, β is the coefficient of volumetric thermal expansion, $c(\mathbf{r})$ is the acoustic speed distribution and C_p is the specific heat. Usually the density of the object is assumed to be constant. The TAT algorithm is an inverse problem of deriving $A(\mathbf{r})$ from $p(\mathbf{r}, t)$.

In the spherical detection geometry, $p(\mathbf{r}, t)$ is detected along a spherical surface whose radius is r_0 and center is the origin, i.e. $\mathbf{r} = \mathbf{r}_0$. Usually it is supposed that the electromagnetic pulse function is a Dirac delta function and the pulse emission time is the zero time,

i.e. $I(t) = \delta(t)$. If the acoustic speed $c(\mathbf{r})$ is a constant c_0, the time-domain reconstruction formula for this case can be written as (Xu *et al* 2003)

$$A(\mathbf{r}) \approx -\eta \iint_{\Omega_0} \mathrm{d}\Omega_0 \frac{1}{|\mathbf{r}-\mathbf{r}_0|} \frac{\partial p(\mathbf{r}_0, t)}{\partial t}\bigg|_{t=|\mathbf{r}_0-\mathbf{r}|/c_0} \tag{2}$$

where η is a constant.

If the acoustic speed is not a constant, no direct inverse formula can be proposed. Nevertheless, the physical meaning of (2), described as follows, is enlightening. The thermoacoustic wave generated by the tissue at the position $\mathbf{r}$ reaches the ultrasonic transducer position $\mathbf{r}_0$ at the time t. So $A(\mathbf{r})$ can be calculated by the backprojection $(1/|\mathbf{r}-\mathbf{r}_0|) \cdot (\partial p(\mathbf{r}_0, t)/\partial t)$ of all detected signals over the spherical surface at the corresponding time t. If the acoustic speed is homogeneous, t is proportional to the distance between $\mathbf{r}$ and $\mathbf{r}_0$. When the acoustic speed is heterogeneous, t becomes a function of $\mathbf{r}$ and $\mathbf{r}_0$, i.e. $t = T(\mathbf{r}, \mathbf{r}_0)$. Equation (2) can be heuristically modified (Xu and Wang 2003) for use with weakly acoustic heterogeneous media as

$$A(\mathbf{r}) \approx -\eta \iint_{\Omega_0} \mathrm{d}\Omega_0 \frac{1}{|\mathbf{r}-\mathbf{r}_0|} \frac{\partial p(\mathbf{r}_0, t)}{\partial t}\bigg|_{t=T(\mathbf{r},\mathbf{r}_0)}. \tag{3}$$

Equation (3) is our approximate inverse formula for TAT with the compensation for the inhomogeneous acoustic speed. Considering the acoustic speed in biological soft tissues is normally weakly heterogeneous, this formula ignores the effect of acoustic amplitude distortions introduced by the acoustic wave refraction, which would require a modified backprojection coefficient rather than $1/|\mathbf{r}-\mathbf{r}_0|$. As such, the error of (3) will increase if the acoustic speed heterogeneity is stronger.

In (3), $T(\mathbf{r}, \mathbf{r}_0)$ can be calculated by (Snieder and Aldridge 1995, Xu and Wang 2003)

$$T(\mathbf{r}, \mathbf{r}_0) \approx \int_l \frac{1}{c(\mathbf{r})} \mathrm{d}s \tag{4}$$

where l is the line path between $\mathbf{r}$ and $\mathbf{r}_0$, that is the acoustic path without the acoustic speed variation. Equation (4) compensates for the first-order travel time perturbation, the effect of the acoustic speed heterogeneity along l, and neglects the high order perturbation, the effect of acoustic wave refraction.

In fact, the acoustic speed distribution $c(\mathbf{r})$ is normally unknown in practical applications, and so is $T(\mathbf{r}, \mathbf{r}_0)$. In such cases, it would confront the problem of non-uniqueness while using detected thermoacoustic signals to reconstruct $A(\mathbf{r})$ and $c(\mathbf{r})$ simultaneously. For instance, if the detected object is a point, all detected thermoacoustic signals become the differential of the Dirac delta function. Obviously, there exists countless $c(\mathbf{r})$ that could result in thermoacoustic signals with a given arrival time at each detection position. However, considering that the attenuation of acoustic waves is proportional to $1/r$ (ignoring the dissipative effect), it is still possible to identify the location of the point by analyzing different amplitudes of detected signals, which suggest the point's relative distances from all detection positions. This implies that the correlation between thermoacoustic signals could be utilized to compensate for the acoustic heterogeneity even if the acoustic speed distribution is unknown. Accordingly, a correlation-based method is proposed to estimate $T(\mathbf{r}, \mathbf{r}_0)$ in the next section.

2.2. *Estimation of* $T(\mathbf{r}, \mathbf{r}_0)$

The detected thermoacoustic wave can be written as (Jin and Wang 2006)

$$p(\mathbf{r}_0, t) \approx \eta_2 \frac{\partial}{\partial t} \iint_{\Omega_0} \frac{A(\mathbf{r})}{|\mathbf{r}-\mathbf{r}_0|} \mathrm{d}\Omega_0\bigg|_{T(\mathbf{r},\mathbf{r}_0)=t} \tag{5}$$

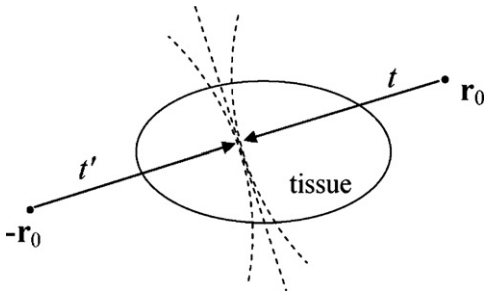

Figure 1. The tissue's corresponding parts of thermoacoustic signals detected at $\mathbf{r}_0$ and $-\mathbf{r}_0$.

where η_2 is a constant. Here $S(\mathbf{r}_0, t)$ is defined as

$$S(\mathbf{r}_0, t) = \left[\int_0^t p(\mathbf{r}_0, t)\,\mathrm{d}t\right] \cdot t \approx \eta_2 \iint_{\Omega_0} \frac{t}{|\mathbf{r} - \mathbf{r}_0|} A(\mathbf{r})\,\mathrm{d}\Omega_0 \Big|_{T(\mathbf{r},\mathbf{r}_0)=t}. \tag{6}$$

In (6), each point on the integral surface Ω_0 has the same time-of-flight t from $\mathbf{r}_0$. If $c(\mathbf{r})$ is homogeneous, Ω_0 is simplified to a sphere surface and $t/|\mathbf{r} - \mathbf{r}_0|$ is a constant. As shown in figure 1, when the size of the detected tissue is relatively small compared to r_0, Ω_0 can be approximated to a plane. Then it is obvious that

$$S(\mathbf{r}_0, t) \approx S(-\mathbf{r}_0, t') \tag{7}$$

where $t + t' = T(-\mathbf{r}_0, \mathbf{r}_0)$, because $S(\mathbf{r}_0, t)$ and $S(-\mathbf{r}_0, t')$ correspond to the same integral plane. The error of (7) will be enlarged if the acoustic speed heterogeneity is enhanced or the tissue is relatively larger.

It is implied by (7) that there is a strong correlation between thermoacoustic signals detected at origin-symmetric positions. So an efficient way to calculate $T(-\mathbf{r}_0, \mathbf{r}_0)$ is that

$$T(-\mathbf{r}_0, \mathbf{r}_0) = \arg\max(R_{\mathbf{r}_0}(t)) \tag{8}$$

where $R_{\mathbf{r}_0}(t)$ is the correlation function of $S(\mathbf{r}_0, t)$ and $S(-\mathbf{r}_0, -t)$, defined as

$$R_{\mathbf{r}_0}(t) = \int_{-\infty}^{\infty} S(\mathbf{r}_0, \tau) S(-\mathbf{r}_0, -(\tau - t))\,\mathrm{d}\tau \tag{9}$$

where $S(\mathbf{r}_0, t)$ is zero if $t < 0$. Supposing the acoustic speed between $\mathbf{r}_0$ and $-\mathbf{r}_0$ is approximately homogeneous,

$$T(k \cdot \mathbf{r}_0, \mathbf{r}_0) \approx \frac{|1 - k|}{2} \cdot T(-\mathbf{r}_0, \mathbf{r}_0) \tag{10}$$

where $|k| < 1$. Moreover, if the size of the detected tissue is relatively small, the tissue's points with the same distance as $\mathbf{r}_0$ approximately have the same time-of-flight from $\mathbf{r}_0$. Then $T(\mathbf{r}, \mathbf{r}_0)$ can be calculated by

$$T(\mathbf{r}, \mathbf{r}_0) \approx T\left(\mathbf{r}_0 - \frac{|\mathbf{r} - \mathbf{r}_0|}{r_0} \cdot \mathbf{r}_0, \mathbf{r}_0\right) \approx \frac{|\mathbf{r} - \mathbf{r}_0|}{2r_0} \cdot T(-\mathbf{r}_0, \mathbf{r}_0). \tag{11}$$

In summary, using (3), (8) and (11), we can reconstruct the image of a tissue with compensation for acoustic speed variations. First, the acoustic travel time $T(\mathbf{r}, \mathbf{r}_0)$ is estimated by (8) and (11) using the correlation information between thermoacoustic signals detected at origin-symmetric positions. Then the absorbed energy density $A(\mathbf{r})$ is reconstructed using the corrected time-domain formula (3). Theoretically, the larger the detected tissue or the stronger the acoustic speed heterogeneity, the greater the error of this algorithm. The error degree is analyzed in the following simulation studies.

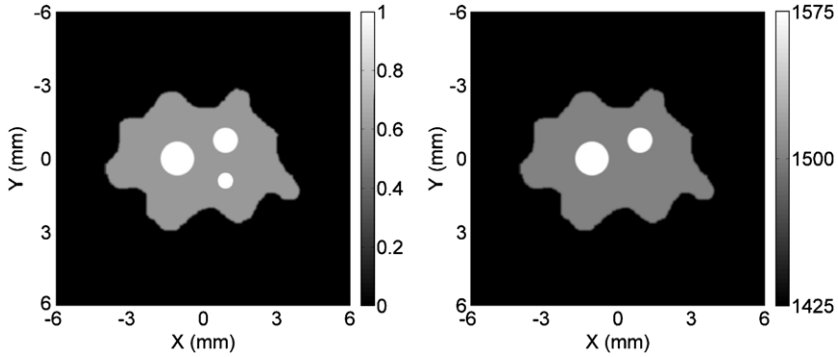

Figure 2. The absorbed energy density (a) and the acoustic speed distribution (b) of the simulated tissue.

3. A simulation method

In order to simulate the thermoacoustic wave p in a medium with the nonlinear acoustic property, a simulation method is presented based on the finite-difference time-domain (FDTD) method, which has been widely used in simulation studies of electromagnetic waves and acoustic waves. In the FDTD method, parameters in (1) are discretized, and then (1) can be expressed as difference equations. So we can finally obtain p by the numerical method.

The excitation source I in TAT, a short pulse with a very broad frequency band, calls for extremely dense meshes in the FDTD method. However, in practical applications of TAT, ultrasonic transducers whose center frequency is of the order of MHz are commonly employed. So there is no need to model frequencies higher than the bandwidth of the detector. Here the detected acoustic signal is $p * h$, where h is the impulse response of the ultrasonic transducer and $*$ represents the convolution. It can be derived from (1) that

$$\nabla^2(p * h) - \frac{1}{c^2}\frac{\partial^2(p * h)}{\partial t^2} = -\frac{\beta}{C_p}A \cdot \frac{\partial(I * h)}{\partial t}. \tag{12}$$

Equation (12) shows that the detected acoustic signal equals the FDTD result when using $I * h$ as the impulse source. Because high frequency components of I are filtered by h, better precision can be achieved within the FDTD simulation even using relatively sparse meshes.

In the simulation study, thermoacoustic signals of the tissue are first calculated by the FDTD method. Then the tissue image is reconstructed from simulated signals. The simulation is conducted in the 2D case, whose conclusions can be extended straightforwardly to the 3D case, to reduce the computational complexity.

The absorbed energy density and acoustic speed (m s^{-1}) distribution of the simulated tissue are shown in figures 2(a) and (b), respectively. The interface geometries of the absorbed energy density and acoustic speed distribution are set to be slightly different (seeing the minimum circle), which may occur in practical situations. This type of inhomogeneous acoustic speed distribution is similar to the acoustic model of the female breast (Xu and Wang 2003). The acoustic speed of the background (representing the subcutaneous fat and matching media in which the object is imbedded) is 1425 m s^{-1}, the acoustic speed inside the irregular boundary (representing the breast parenchyma) is 1500 m s^{-1}, and the acoustic speed inside two circles (representing tumors although larger than the usual ones) is 1575 m s^{-1}. Generated thermoacoustic signals are calculated by the FDTD method, in which the space interval is set

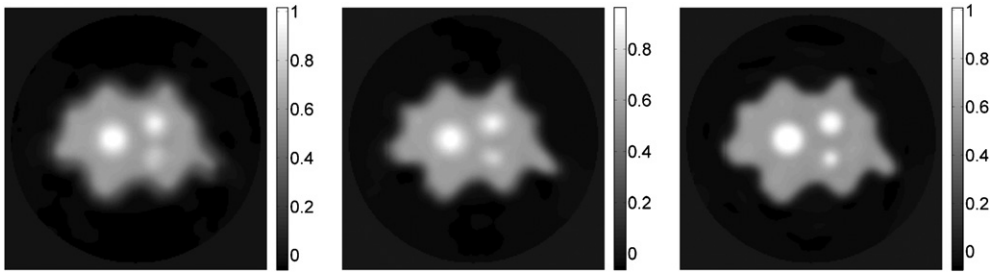

(a) (b) (c)

Figure 3. Reconstructed images, using (a) $c = 1470$ m s^{-1}, (b) $c = 1425$ m s^{-1} and (c) the prior known $c(\mathbf{r})$.

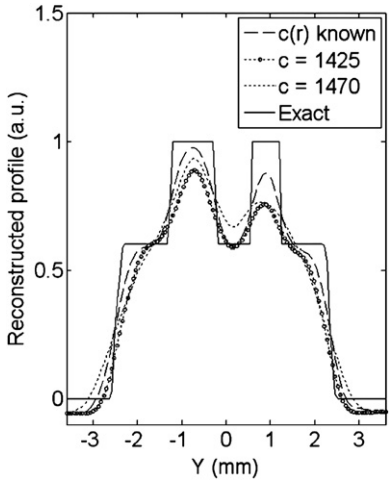

Figure 4. Profiles through reconstructed images (figure 3) along $x = 0.9$ mm.

to 0.03 mm and the time interval is set to 5 ns. Thermoacoustic signals are detected at 240 positions equally distributed along a circle whose center is at (0, 0) and radius is 9 mm.

4. Results and discussions

Reconstructed images using different fixed c by the time-domain formula (2) are shown in figures 3(a) and (b) (with the same coordinate of figure 2), and the reconstructed image using prior-known inhomogeneous $c(\mathbf{r})$ and the corrected formula (3) is shown in figure 3(c). It can be seen that the result of our inverse formula is better than those using the homogeneous c with clearer boundaries. The smallest object in the tissue is reconstructed clearly only in figure 3(c).

Profiles through reconstructed images in figure 3 along $x = 0.9$ mm are shown in figure 4. Obviously, the result of (3) is quantitatively more accurate than those without the compensation for acoustic variations. However, the reconstructed peak pixel value of the smallest object is still smaller than the exact value, because (3) is not an exact inverse formula.

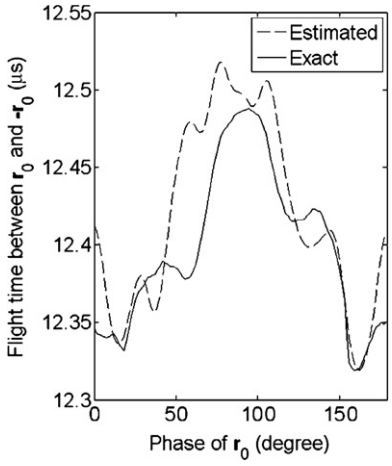

Figure 5. The estimated flight time between $\mathbf{r}_0$ and $-\mathbf{r}_0$.

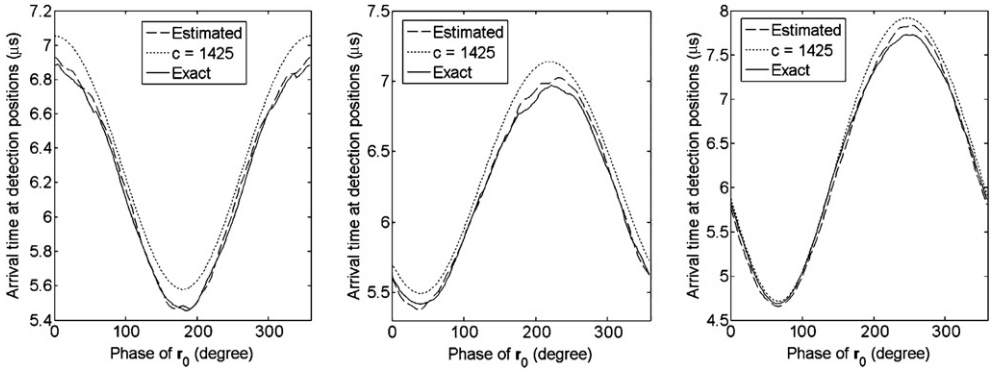

Figure 6. Estimated acoustic arrival time to detection positions: (a) point A, (b) point B and (c) point C.

In practical applications, the acoustic speed distribution $c(\mathbf{r})$ is normally unknown. So $T(\mathbf{r}, \mathbf{r}_0)$, required in (3), is estimated by (8) and (11). First, $T(-\mathbf{r}_0, \mathbf{r}_0)$ is calculated by (8) and the result is shown in figure 5. The phase of $\mathbf{r}_0$ is defined by the coordinate (x, y) of figure 2 as follows; (6, 0) is 0°, (0, −6) is 90° and so forth. The exact value of $T(-\mathbf{r}_0, \mathbf{r}_0)$ is given by (4), which is precise enough in this case of weak acoustic heterogeneity. As shown in figure 5, the estimated $T(-\mathbf{r}_0, \mathbf{r}_0)$ is in accordance with the trend of speed variations, and therefore could be utilized to compensate for the acoustic heterogeneity.

Then $T(\mathbf{r}, \mathbf{r}_0)$ is calculated by (11). The acoustic arrival times from three points to detection positions are shown in figure 6. These three points, defined as A, B and C, are the centers of the three circles in figure 2(a). A is at (−1.05, 0), B is at (0.9, −0.75) and C is at (0.9, 0.9). Results of assumed homogeneous acoustic speed (1425 m s^{-1}) are also shown in figure 6. Obviously the estimated $T(\mathbf{r}, \mathbf{r}_0)$ of our method is more precise than those derived from fixed acoustic speeds.

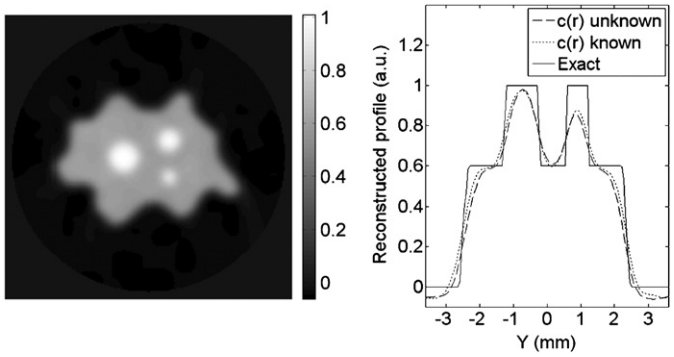

(a) (b)

Figure 7. The reconstructed image (a) and the reconstructed profile along $x = 0.9$ mm (b) when $c(\mathbf{r})$ is unknown.

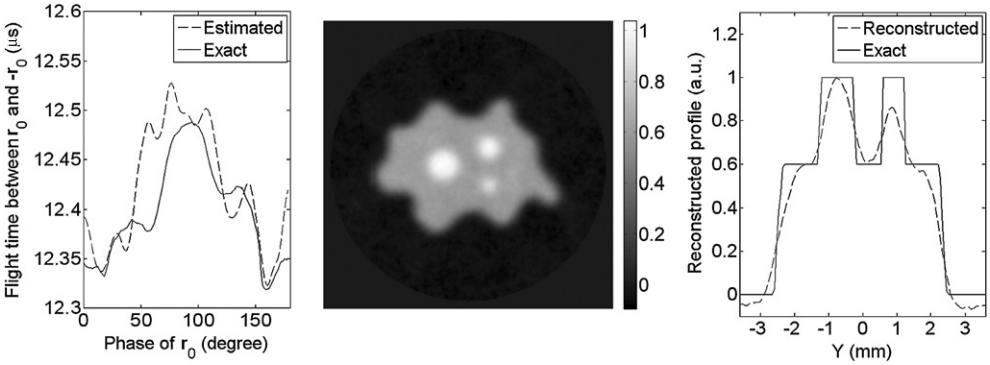

(a) (b) (c)

Figure 8. Reconstructed results from noisy thermoacoustic signals (SNR = 10 dB): (a) estimated $T(-\mathbf{r}_0, \mathbf{r}_0)$, (b) reconstructed image and (c) reconstructed profile along $x = 0.9$ mm.

The reconstructed image based on the estimated $T(\mathbf{r}, \mathbf{r}_0)$, as shown in figure 7(a), has a good precision. The smallest object could be identified clearly. Figure 7(b) shows reconstructed profiles through figures 7(a) and 3(c) along $x = 0.9$ mm. It can be seen that the two objects' location and absorbed energy density reconstructed by our estimation-based method are nearly the same as those while $c(\mathbf{r})$ is already known and are close to exact values.

In order to testify this algorithm's robustness to noise, thermoacoustic signals are added with zero-mean Gaussian noises. Then images are reconstructed based on thermoacoustic signals with the signal-to-noise ratio (SNR) of 20 dB, 15 dB and 10 dB. The estimated $T(-\mathbf{r}_0, \mathbf{r}_0)$, reconstructed image and reconstructed profile are shown in figures 8(a)–(c) respectively, while the SNR of thermoacoustic signals is the lowest, i.e. 10 dB. It can be found that this algorithm is not sensitive to random data noises under our simulation condition. Here some realistic effects such as the finite sampling and the positioning error are not investigated. To carry out this algorithm with the experimental data may be the most convincing way to test its noise sensitivity and will be included in our further study.

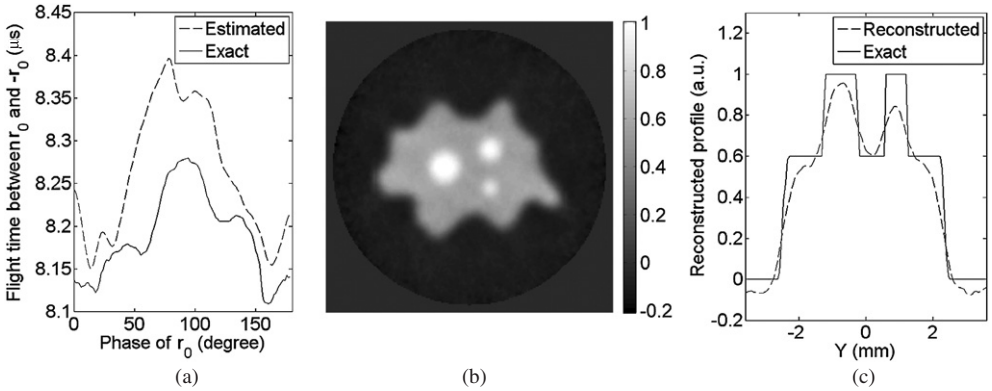

(a) (b) (c)

Figure 9. Reconstructed results with the scanning radius of 6 mm (from noisy data): (a) estimated $T(-\mathbf{r}_0, \mathbf{r}_0)$, (b) reconstructed image and (c) reconstructed profile along $x = 0.9$ mm.

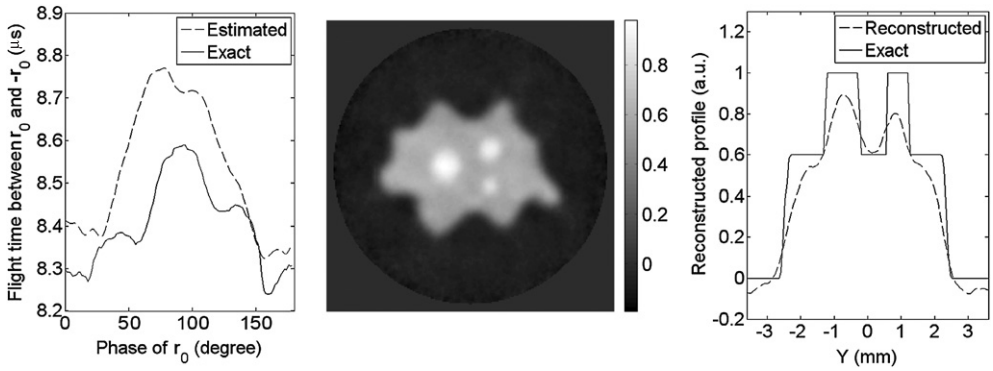

(a) (b) (c)

Figure 10. Reconstructed results while the acoustic variation is 20% (from noisy data): (a) estimated $T(-\mathbf{r}_0, \mathbf{r}_0)$, (b) reconstructed image and (c) reconstructed profile along $x = 0.9$ mm.

According to the theory in section 2, the larger the size of the detected tissue compared to the scanning radius, the greater the error of our algorithm. Here the scanning radius is reduced to 6 mm, and the estimated $T(-\mathbf{r}_0, \mathbf{r}_0)$, reconstructed image and reconstructed profile (from noisy data, SNR = 10 dB) are shown in figures 9(a)–(c), respectively. Comparing figure 9 with figure 8, it can be found that the error is enhanced. Nevertheless, all objects could still be identified.

The degree of acoustic heterogeneity is enlarged as a further justification of this algorithm. In previous cases the acoustic speed variation is about 10% as shown in figure 2(b). Here the speed variation is increased to 20% (the acoustic speed of the background is reduced to 1350 m s^{-1}, the acoustic speed inside two circles is increased to 1650 m s^{-1}). The estimated $T(-\mathbf{r}_0, \mathbf{r}_0)$, reconstructed image and reconstructed profile (from noisy data, SNR = 10 dB) are shown in figures 10(a)–(c), respectively, while the scanning radius is still 6 mm. Comparing figure 10 with figure 9, it can be found that the error increases while the acoustic heterogeneity is enlarged.

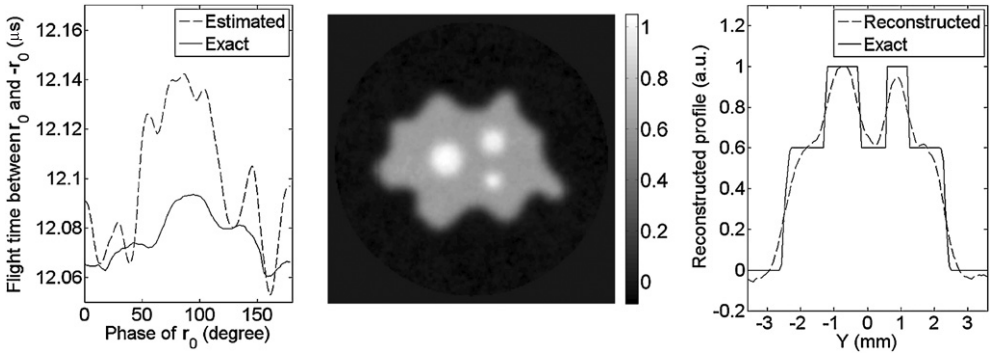

(a) (b) (c)

Figure 11. Reconstructed results while the acoustic variation is 2% (from noisy data): (a) estimated $T(-\mathbf{r}_0, \mathbf{r}_0)$, (b) reconstructed image and (c) reconstructed profile along $x = 0.9$ mm.

Finally, an extreme case was presented in which the speed variation in figure 2(b) is reduced to be as slight as 2% (the acoustic speed of the background is 1485 m s^{-1}, the acoustic speed inside two circles is 1515 m s^{-1}) and the scanning radius is relatively large (9 mm). According to the theory, the reconstruction in this case should be more accurate than those in previous cases. The estimated $T(-\mathbf{r}_0, \mathbf{r}_0)$, reconstructed image and reconstructed profile (from noisy data, SNR = 10 dB) are shown in figures 11(a)–(c), respectively. It can be found that the reconstructed image is better than those in figures 8–10 (it is worth noting that the y-axis interval of figure 11(a) is set to be very small so the estimated curve is not close to the exact one). The reconstructed peak pixel value of the smallest object is very close to the exact value. The remaining errors of the reconstructed smallest object and the smoothing of reconstructed edges may be due largely to the limited frequency band of the FDTD-based simulation method. The cutoff frequency of the FDTD simulation is about 5 MHz and the loss of high frequency signals will result in such errors and effects (Xu *et al* 2003). In fact, when the acoustic variation is so slight, reconstruction algorithms without the compensation for the acoustic speed homogeneity could also achieve a good result. Here the result of our algorithm is presented mainly to corroborate the basic theory.

In summary, this algorithm has a good accuracy and is not sensitive to random noises. Although it is an approximate one, the algorithm is proven to work well under an irregular geometry of the acoustic speed distribution by our simulation studies. The error of this algorithm is mainly focused on the reconstructed pixel values of objects, yet reconstructed positions are always accurate. Moreover, the error increases while the tissue size is larger (compared with the scanning radius) or the acoustic heterogeneity is greater. Generally, if the acoustic speed variation is within 10%, the reconstructed image has a good quality even if the tissue size is close to the scanning radius. In most biological soft tissues, the acoustic speed variation may be within 10%. So this algorithm is suitable for TAT of biological soft tissues.

The reconstruction of an image (200 × 200) by this algorithm is within 10 s on a 2.0 GHz Pentium 4 computer. This is much faster than the FE method, which is reported to cost more than 2 h to reconstruct an image (Jiang *et al* 2006). To the best of our knowledge, the FE method is so far the only algorithm, which does not need the prior knowledge of the acoustic speed distribution, for TAT with the compensation for the acoustic heterogeneity. The advantage of the FE method to our algorithm is that it can reconstruct the acoustic speed distribution. However, this is not necessary as long as the absorbed energy density is reconstructed with a good precision, such as in our algorithm.

In fact, in TAT nearly all algorithms with the compensation for the acoustic heterogeneity are based on forward models and update the image iteratively. No matter whether the acoustic speed distribution is known or not, our inverse algorithm could render a good initial guess for these model-based algorithms. Accordingly, in those cases where our algorithm could not reconstruct a good image (perhaps resulting from a severe acoustic heterogeneity or highly complicated geometry of acoustic speed), it may be an efficient approach to combine our algorithm with other model-based algorithms.

5. Conclusion

An inverse reconstruction algorithm is proposed for TAT with the compensation for the inhomogeneous acoustic speed. The correlation information between thermoacoustic signals is used to compensate for the acoustic speed heterogeneity. Simulation results show that the algorithm is quite precise within the acoustic speed variation of 10%, not sensitive to random data noises and much more computationally efficient than the FE method. The acoustic speed variation in most biological soft tissues is lower than 10%, so this algorithm is suitable for practical applications.

Acknowledgments

This work was supported by the National Basic Research Program of China (No. 2006CB705707), Natural Science Foundation of China (No. 30570488) and Shanghai Leading Academic Discipline Project (No. B112).

References

Anastasio M A, Zhang J and Pan X 2005a Image reconstruction in thermoacoustic tomography with compensation for acoustic heterogeneities *Proc. SPIE* **5750** 298–304

Anastasio M A, Zhang J, Pan X, Zou Y, Ku G and Wang L V 2005b Half-time image reconstruction in thermoacoustic tomography *IEEE Trans. Med. Imaging* **24** 199–210

Fang H, Maslov K and Wang L V 2007 Photoacoustic Doppler effect from flowing small light-absorbing particles *Phys. Rev. Lett.* **99** 184501-1-4

Guo B, Li J, Zmuda H and Sheplak M 2007 Multifrequency microwave-induced thermal acoustic imaging for breast cancer detection *IEEE Trans. Ultrason. Ferroelectr. Freq. Control* **54** 2000–10

Jiang H, Yuan Z and Gu X 2006 Spatially varying optical and acoustic property reconstruction using finite-element-based photoacoustic tomography *J. Opt. Soc. Am.* A **23** 878–88

Jin X and Wang L V 2006 Thermoacoustic tomography with correction for acoustic speed variations *Phys. Med. Biol.* **51** 6437–48

Kostli K P and Beard P C 2003 Two-dimensional photoacoustic imaging by use of Fourier-transform image reconstruction and a detector with an anisotropic response *Appl. Opt.* **42** 1899–908

Kruger R A, Liu P, Fang Y and Appledom C R 1995 Photoacoustic ultrasound (PAUS)-reconstruction tomography *Med. Phys.* **22** 1605–9

Kruger R A, Miller K D, Raynolds H E, Kiser W L, Reinecke D R and Kruger G A 2000 Breast cancer in vivo: contrast enhancement with thermoacoustic CT at 434 MHz—feasibility study *Radiology* **216** 279–83

Kunyansky L A 2007 Explicit inversion formulae for the spherical mean Radon transform *Inverse Problems* **23** 373–83

Niederhauser J J, Jaeger M, Lemor R, Weber P and Frenz M 2005 Combined ultrasound and optoacoustic system for real-time high-contrast vascular imaging in vivo *IEEE Trans. Med. Imaging* **24** 436–40

Snieder R and Aldridge D F 1995 Perturbation theory for travel times *J. Acoust. Soc. Am.* **98** 1565–9

Wang X, Pang Y, Ku G, Xie X, Stoica G and Wang L V 2003 Noninvasive laser-induced photoacoustic tomography for structural and functional *in vivo* imaging of the brain *Natl. Biotechnol.* **21** 803–6

Xu M and Wang L V 2006 Photoacoustic imaging in biomedicine *Rev. Sci. Instrum.* **77** 041101–1-22

Xu M, Xu Y and Wang L V 2003 Time-domain reconstruction algorithms and numerical simulations for thermoacoustic tomography in various geometries *IEEE Trans. Biomed. Eng.* **50** 1086–99

Xu Y and Wang L V 2003 Effects of acoustic heterogeneity in breast thermoacoustic tomography *IEEE Trans. Ultrason. Ferroelectr. Freq. Control* **50** 1134–46

Zhang H F, Maslov K, Stoica G and Wang L V 2006 Functional photoacoustic microscopy for high-resolution and noninvasive *in vivo* imaging *Natl. Biotechno.* **24** 848–51

Zhang J and Anastasio M A 2006 Reconstruction of speed-of-sound and electromagnetic absorption distributions in photoacoustic tomography *Proc. SPIE* **6080** 608619–1-7